AIAA SciTech Forum
12-16 January 2026, Orlando, FL
AIAA SCITECH 2026 Forum

10.2514/6.2026-2716

Thrust Vector Control for Flexible Launch Vehicles: An $\mathcal{H}_\infty$ Open Loop Shaping Approach

João T. Diz*
Delft University of Technology, Kluyverweg 1, 2629 HS Delft, The Netherlands

Spilios Theodoulis †
Delft University of Technology, Kluyverweg 1, 2629 HS Delft, The Netherlands

Pedro Simplício‡
European Space Agency, Keplerlaan 1, 2201 AZ Noordwijk, Netherlands.

This paper continues previous work on the application of $\mathcal{H}_\infty$ Open Loop Shaping (OLS) to the design of thrust vector control (TVC) systems for launch vehicles (LVs). The contributions are threefold: first, further insight is provided into the selection and role of weighting filters within the loop shaping step; second, through two examples, it is shown that $\mathcal{H}_\infty$ OLS and $\mathcal{H}_\infty$ Closed Loop Shaping (CLS) result in equivalent controllers for rigid LVs, with neither approach outperforming the other; third, the $\mathcal{H}_\infty$ OLS methodology is extended to flexible LVs, introducing a simultaneous attitude controller and bending filter design strategy. Compared to $\mathcal{H}_\infty$ CLS, $\mathcal{H}_\infty$ OLS simplifies the design process by avoiding the simultaneous tuning of multiple closed loop transfer functions and ensuring robustness at the plant input and output. These advantages, combined with the demonstrated performance parity, support the use of $\mathcal{H}_\infty$ OLS for LV control applications. The flexible OLS framework was also benchmarked against the traditional separate design method, yielding similar results with reduced workload. Additionally, using the integrated approach in combination with a multi-model framework, a controller was developed and validated through linear simulations under both nominal and dispersed conditions, satisfying all TVC system performance and robustness requirements. Future work will address sloshing dynamics and develop a full-envelope controller for nonlinear simulation to further consolidate the methodology's applicability.

I. Introduction

Launch vehicles (LVs) are the cornerstone of space exploration, satellite deployment, scientific research, and national security operations. Access to space is not only crucial for expanding our understanding of the universe, but also for driving technological innovation, promoting economic development, and strengthening international cooperation. As the demand for space access increases—driven by the rise of satellite constellations, commercial space ventures, and global collaboration—the need for more frequent and reliable launch services becomes increasingly evident.

A critical subsystem of LVs is the Thrust Vector Control (TVC) system, part of the Guidance, Navigation, and Control (GNC) architecture. The TVC system adjusts the direction of engine thrust to control the vehicle's attitude, ensuring stability, tracking guidance commands, and rejecting disturbances from atmospheric uncertainties and structural dynamics. Designing the TVC control system is a complex task: most launch vehicles are aerodynamically unstable [1]; the controller must address multiple competing requirements, such as attitude tracking, load alleviation, and actuation minimization [2]; the vehicle exhibits non-negligible structural flexibility [3]; and the system is highly time-varying [1].

The traditional approach to designing the TVC control system — which is composed of a rigid body controller (attitude controller) and a bending filter — has proven effective in managing these challenges. However, it presents several limitations [1]: the design process is time-consuming, it struggles to address multivariable problems, and possesses no explicit way to address uncertainty - stability robustness is enforced only through gain and phase margins.

Over time, advancements in TVC system design have moved beyond the classical approach to include modern control approaches. Early efforts incorporated optimal control techniques, such as the use of the Linear Quadratic

*Graduate Student, Control & Simulation Section, Faculty of Aerospace Engineering, Student AIAA Member.
†Associate Professor, Control & Simulation Section, Faculty of Aerospace Engineering, Associate Fellow AIAA Member
‡GNC Engineer, European Space Agency.

Gaussian (LQG) method in the development of Ariane V's initial rigid body controller [4]. While optimal control improved the handling of multivariable systems and reduced design time, it suffered from notable drawbacks, including the absence of guaranteed stability margins at the plant's input and output [5].

These limitations motivated the adoption of robust control, a framework well-suited to aerospace applications due to its inherent ability to manage system uncertainties, support multivariable design, and streamline the synthesis process. Among the various robust control methods, $\mathcal{H}_\infty$ Closed Loop Shaping (CLS) has received considerable attention in the context of launch vehicle TVC system design. This method focuses on shaping the system's closed-loop transfer functions (CLTFs) to achieve performance and robustness objectives. Compared to earlier approaches, $\mathcal{H}_\infty$ CLS provides a more systematic way to incorporate design specifications, as demonstrated in studies such as [1].

However, as discussed in [6], $\mathcal{H}_\infty$ CLS is not without limitations. Achieving robustness at both the plant input and output requires the simultaneous shaping of multiple CLTFs, a process that can become cumbersome and complex. Moreover, conflicting performance objectives often arise while shaping the CLTFs, making the tuning process challenging and increasing the overall design complexity.

In [6], the authors proposed the use of $\mathcal{H}_\infty$ Open Loop Shaping (OLS), a method within the robust control framework, as an alternative to $\mathcal{H}_\infty$ CLS for the design of launch vehicle attitude controllers. This work systematized the use of $\mathcal{H}_\infty$ OLS, simplifying its application to the selection of five weighting filters (three first-order filters and two gains) for the initial controller design, and to setting two gains for subsequent flight points. This methodology not only automatically achieves robustness at both the plant input and output, but also eliminated the need to simultaneously shape multiple transfer functions. Preliminary results in [6] showed that $\mathcal{H}_\infty$ OLS and $\mathcal{H}_\infty$ CLS produced nearly identical controllers, with $\mathcal{H}_\infty$ OLS offering the simpler approach.

This paper builds upon the work presented in [6]. The contributions of this paper are threefold: first, it provides further insights into the weighting filter parametrization described in the previous work; second, it extends the comparison between $\mathcal{H}_\infty$ CLS and $\mathcal{H}_\infty$ OLS, providing two examples that illustrate how one method does not outperform the other; and third, it extends the $\mathcal{H}_\infty$ OLS methodology to account for the flexible launch vehicle case, resulting in a Simultaneous Attitude Controller/Bending Filter $\mathcal{H}_\infty$ OLS design strategy.

The paper is structured as follows. In Section II, the open loop model used in this study is described, along with the requirements used for the flight control system. Section III outlines the general $\mathcal{H}_\infty$ Open Loop Shaping strategy. Section IV revisits the weighting filter parametrization from [6] and provides further insights into the role of each weighting filter. Section V presents two comparison examples between $\mathcal{H}_\infty$ CLS and $\mathcal{H}_\infty$ OLS. Section VI details the Simultaneous Attitude Controller/Bending Filter design strategy, compares it to the separate design approach, describes the computation of a multi-model-based controller using the simultaneous design strategy, and presents frequency-domain and time-domain results for the simultaneous design controllers. Finally, Section VII provides the conclusions of this work.

II. Launch Vehicle Model and Attitude Control Requirements

The flexible launch vehicle open loop model is constructed by combining the Linear-Time-Invariant (LTI) system, which describes the flexible motion of the LV, with a delay model that captures the time delay introduced by the on-board digital units, and an actuator model. These components are detailed in Subsections II.A, II.B, and II.C. Having described the LV model, the requirements for attitude control are described in Subsection II.D.

It should be noted that all the models are populated using data representative of Europe's small launcher (VEGA), corresponding to the flight point at which the dynamic pressure is highest. The uncertainty ranges for the flexible parameters are also representative of this launcher. For the non-flexible parameters, uncertainty levels were defined following the approach in [7]: 20% for aerodynamic parameters, 2% for mass, inertia, and center of mass, and 10% for the rest.

A. Launch Vehicle LTI Model

The LTI model of the flexible launch vehicle is derived under the assumptions of axial symmetry and negligible roll rate effects. These assumptions enable the decoupling of the yaw and pitch axes, which are also considered identical. As a result, the analysis can be restricted to the pitch plane, eliminating yaw and lateral motion in the yaw plane as degrees of freedom. Furthermore, by neglecting the longitudinal dynamics—since they are minimally influenced by small perturbations [8]—and assuming the use of a gravity-turn manoeuvre, an LTI system can be constructed and linearized around the local trajectory reference frame.

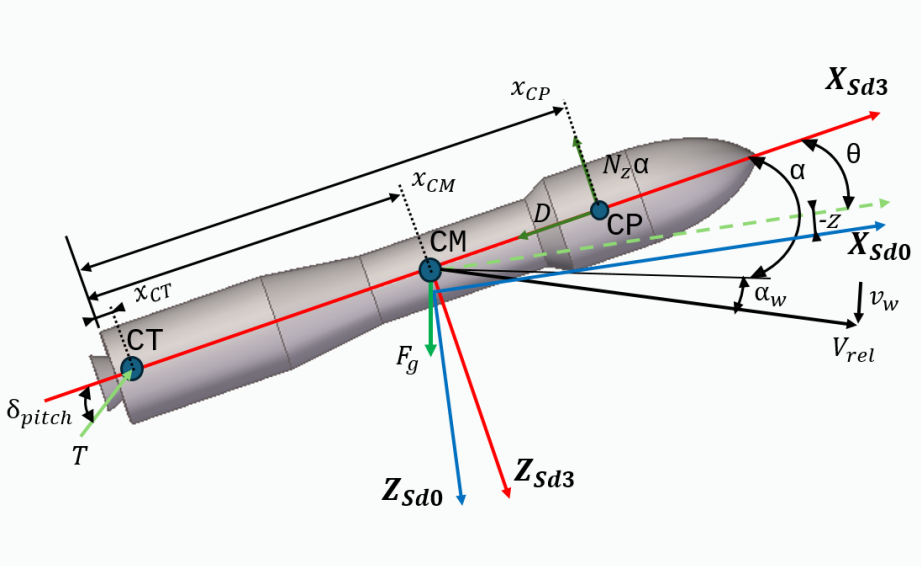

Fig. 1 LV - Rigid body diagram - pitch plane.

In this work, thrust, gravity, aerodynamic forces, engine inertia, and LV bending motion are considered significant to the vehicle's motion. Accordingly, the translational and rotational equations are formulated as follows:

$$\begin{aligned} m\ddot{z} =& -(T-D)\theta + N\left(\theta + \frac{\dot{z}}{V} + \frac{v_w}{V} - \frac{\dot{\theta}}{V}l_{CP}\right) - T\delta_{pitch} - m_n l_n \ddot{\delta}_{pitch} + F_{flex} \\ I_{yy}\ddot{\theta} =& N l_{CP}\left(\theta + \frac{\dot{z}}{V} + \frac{v_w}{V} - \frac{\dot{\theta}}{V}l_{CP}\right) - T\delta_{pitch} l_{CG} - (m_n l_n l_{CG} + I_n)\,\ddot{\delta}_{pitch} + M_{flex} \end{aligned} \tag{1}$$

where T is the thrust force, D is the drag force, F_{flex}, and M_{flex} represent the contributions from the LV's bending modes, and V is the vehicle velocity with respect to ground. θ, $\dot{\theta}$, z, and $\dot{z}$ represent pitch angle, pitch rate, drift, and drift rate, respectively. m_n and l_n represent the mass of the nozzle and the distance between the nozzle's center of mass and the center of thrust, respectively. δ_{pitch} denotes the deflection of the nozzle. m and I_{yy} are the mass and moment of inertia of the LV, respectively. x_{CM}, x_{CP}, and x_{CT} denote the distances from the bottom edge of the LV to the center of mass, center of pressure, and center of thrust, respectively. The distances $l_{CM} = x_{CM} - x_{CT}$ and $l_{CP} = x_{CP} - x_{CT}$ are the lever arms from the center of thrust to the center of mass and center of pressure, respectively, and can be visualized in Figure 1. In this figure, $Sd0$ and $Sd3$ represent the local trajectory reference frame and body frame, respectively.

The contribution from the bending modes can be described by the following equations:

$$\begin{aligned} F_f &= T\sum_{i=1} \frac{\partial \Psi_i(x_{CT})}{\partial x} q_i \\ M_f &= -T\left((x_{CM} - x_{CT})\right)\sum_{i=1}^{k} \frac{\partial \Psi_i(x_{CT})}{\partial x} q_i + \sum_{i=1}^{k} \Psi_i(x_{CT}) q_i \end{aligned} \tag{2}$$

where Ψ_i represents the Translational Length of the ith bending mode; $\Psi_i'(x) = \frac{\partial \Psi_i}{\partial x}$ is the Rotational Length of the ith bending mode, and q_i is the generalized coordinate of the ith bending mode (it can represent displacement, elastic torsion, etc).

Considering only the first order effects (for simplicity), the ith bending mode is mainly excited by the LV engine, as stated by [9]. Its dynamics are described by the following equation:

$$\ddot{q}_i + 2\zeta_i\omega_i\dot{q}_i + \omega_i^2 q_i = \left(-T\delta - m_N l_N \ddot{\delta}\right)\Psi_i(x_{CT}) + I_n\ddot{\delta}\frac{\partial \Psi(x_{CT}))}{\partial x} \tag{3}$$

where ω_i is the frequency of the ith bending mode; ζ is the damping of the ith bending mode.

Finally, the effect of the Inertial Measurement Unit (IMU) on the system must be taken into account. On one hand, its location influences the sensor readings; on the other hand, bending motion affects its actual position. These effects are described by the following equations:

$$\theta_{IMU} = \theta - \sum_i q_i \Psi_i' \left(x_{IMU}\right) \tag{4}$$

$$\dot{\theta}_{IMU} = \dot{\theta} - \sum_i \dot{q}_i \Psi_i' \left(x_{IMU}\right) \tag{5}$$

$$z_{IMU} = z - (x_{IMU} - x_{CM})\theta + \sum_{i=1}^{k} q_i \Psi_i(x_{IMU}) \tag{6}$$

$$\dot{z}_{IMU} = \dot{z} - (x_{IMU} - x_{CM})\dot{\theta} + \sum_{i=1}^{k} \dot{q}_i \Psi_i(x_{IMU}) \tag{7}$$

where x_{IMU} represents the position of the IMU sensor.

Integrating eq. 1-7, it is possible to compute the following flexible LV LTI model:

$$\begin{bmatrix} \dot{\theta} \\ \ddot{\theta} \\ \dot{z} \\ \ddot{z} \\ \dot{q} \\ \ddot{q} \end{bmatrix} = \left(\begin{array}{cccc|cc} 0 & 1 & 0 & 0 & 0_{1b} & 0_{1b} \\ \mu_\alpha & -\frac{(x_{CP}-x_{CM})\mu_\alpha}{V_{rel}} & 0 & \frac{\mu_\alpha}{V_{rel}} & f_\theta & 0_{1b} \\ 0 & 0 & 0 & 1 & 0_{1b} & 0_{1b} \\ -\frac{N_z}{m_0} + a_0 & \frac{\mu_\alpha I_{yy}}{m_0 V_{rel}} & 0 & \frac{-N_z}{m_0 V_{rel}} & f_z & 0_{1b} \\ \hline 0_{b1} & 0_{b1} & 0_{b1} & 0_{b1} & 0_{bb} & I_b \\ 0_{b1} & 0_{b1} & 0_{b1} & 0_{b1} & f_{q\ddot{q}} & f_{\dot{q}\ddot{q}} \end{array}\right) \begin{bmatrix} \theta \\ \dot{\theta} \\ z \\ \dot{z} \\ q \\ \dot{q} \end{bmatrix} + \left(\begin{array}{cc} 0 & 0 \\ \mu_c & \mu_c' \\ 0 & 0 \\ -\frac{T}{m_0} & \frac{-m_N l_N}{m_0} \\ \hline 0_{b1} & 0_{b1} \\ f_{\delta\ddot{q}} & f_{\ddot{\delta}\ddot{q}} \end{array}\right) \begin{bmatrix} \delta_{pitch} \\ \ddot{\delta}_{pitch} \end{bmatrix} + \left(\begin{array}{c} 0 \\ -\frac{\mu_\alpha}{V_{rel}} \\ 0 \\ \frac{N_z}{m_0 V_{rel}} \\ \hline 0_{b1} \\ 0_{b1} \end{array}\right) [v_w]$$

$$\begin{bmatrix} \tilde{q}\alpha \\ z_{IMU} \\ \dot{z}_{IMU} \\ \theta_{IMU} \\ \dot{\theta}_{IMU} \end{bmatrix} = \left(\begin{array}{cccc|cc} \tilde{q} & 0 & 0 & \frac{\tilde{q}}{V_{rel}} & 0_{1b} & 0_{1b} \\ -(x_{IMU} - x_{CM}) & 0 & 1 & 0 & f_{qz} & 0_{1b} \\ 0 & -(x_{IMU} - x_{CM}) & 0 & 1 & 0_{1b} & f_{qz} \\ 1 & 0 & 0 & 0 & f_{q\theta} & 0_{1b} \\ 0 & 1 & 0 & 0 & 0_{1b} & f_{q\theta} \end{array}\right) \begin{bmatrix} \theta \\ \dot{\theta} \\ z \\ \dot{z} \\ q \\ \dot{q} \end{bmatrix} + \begin{pmatrix} 0 & 0 \\ 0 & 0 \\ 0 & 0 \\ 0 & 0 \\ 0 & 0 \end{pmatrix} \begin{bmatrix} \delta_{pitch} \\ \ddot{\delta}_{pitch} \end{bmatrix} + \begin{pmatrix} -\frac{\tilde{q}}{V_{rel}} \\ 0 \\ 0 \\ 0 \\ 0 \end{pmatrix} [v_w] \tag{8}$$

where

$$\begin{aligned}
f_\theta &= [f_{\theta 1}, ..., f_{\theta b}] && \text{with} \quad f_{\theta i} = \frac{T}{I_{yy}} \left(\Psi_i'(x_{CT})(x_{CP} - x_{CM}) + \Psi_i(x_{CT})\right) \\
f_z &= [f_{z1}, ..., f_{zb}] && \text{with} \quad f_{zi} = \frac{T}{m_0}(\Psi_i'(x_{CT})) \\
f_{q\ddot{q}} &= \text{diag}(f_{q\ddot{q}1}, ..., f_{q\ddot{q}b}) && \text{with} \quad f_{q\ddot{q}i} = -{\omega_i}^2 \\
f_{\dot{q}\ddot{q}} &= \text{diag}(f_{\dot{q}\ddot{q}1}, ..., f_{\dot{q}\ddot{q}b}) && \text{with} \quad f_{\dot{q}\ddot{q}i} = -2\omega_i\zeta_i \\
f_{\delta\ddot{q}} &= [f_{\delta\ddot{q}1}, ..., f_{\delta\ddot{q}b}]^T && \text{with} \quad f_{\delta\ddot{q}i} = -T\Psi_i(x_{CT}) \\
f_{\ddot{\delta}\ddot{q}} &= [f_{\ddot{\delta}\ddot{q}1}, ..., f_{\ddot{\delta}\ddot{q}b}]^T && \text{with} \quad f_{\ddot{\delta}\ddot{q}i} = I_N\Psi_i'(x_{CT}) - m_N l_N \Psi_i(x_{CT}) \\
f_{qz} &= [f_{qz1}, ..., f_{qzb}] && \text{with} \quad f_{qzi} = \Psi_i(x_{IMU}) \\
f_{q\theta} &= [f_{q\theta 1}, ..., f_{q\theta b}] && \text{with} \quad f_{q\theta i} = -\Psi_i'(x_{IMU})
\end{aligned} \tag{9}$$

Additionally, b represents the number of bending modes, and the rigid lines were used to separate the rigid and flexible contributions.

With the state-space model described in equation 8, and by incorporating sufficient bending modes, it is possible to simulate both the displacement caused by flexible behavior in the IMU position and the flexible forces experienced by the launch vehicle. Following the approach outlined in [1], only the first two bending modes will be included in the model.

B. Delay Model

Launch vehicles experience time delays due to the processing performed by on-board digital units. To account for these delays, a delay model can be employed. The delay model that will be used in this work was retrieved from [1] and is presented below:

$$\frac{\delta_{delayed}}{\delta_{cmd}} = \frac{s^2\tau^2 - s6\tau + 12}{s^2\tau^2 + s6\tau + 12} \tag{10}$$

where τ is the time delay.

C. Actuator Model

For this paper, a second order model will be used to represent the actuators. The equation that describes the second order model is shown next:

$$\frac{\delta_{pitch}}{\delta_{cmd}} = \frac{{\omega_a}^2}{s^2 + 2\zeta_a\omega_a s + \omega_a^2} \tag{11}$$

where ω_a is the natural frequency, and where ζ_a is the damping ratio.

D. Requirement Definition

The typical requirements for a launch vehicle's TVC system during atmospheric ascent are well documented in the literature (e.g. [1], [2] and [3]). In this work, the requirements for the TVC system are based on the aforementioned works and are outlined in Table 1, where the tracking and disturbance rejection requirements are the defined as follows:

TR1 - The controller must be capable of tracking pitch angle commands, achieving zero steady-state error while constraining the transient response in terms of overshoot and maximum rate.

DR1 - The controller must be able to reject external disturbances (e.g. wind gusts) and internal dynamics (bending modes).

The requirements in Table 1 can be further categorized into stability and performance criteria. The stability requirements address both rigid and flexible body behavior, incorporating classical stability margins (gain and phase) for nominal and perturbed conditions.

Table 1 Stability and performance requirements for the TVC control system.

	Requirements	Criterions	Bounds
Stability	Rigid body margins	Low Frequency (LF) Gain Margin (GM)	Nominal $\geq$ 6 dB
			Dispersed $\geq$ 0.5 dB
		High Frequency (HF) GM	Nominal ≤ -6 dB
			Dispersed ≤ -3 dB
		Phase Margin (PM)	Nominal $\geq$ 30 deg
			Dispersed $\geq$ 20 deg
	Flexible body margins	GM_f	Nominal ≤ -3 dB
			Dispersed ≤ -3 dB
		PM_f	Nominal $\geq$ 30 deg
			Dispersed $\geq$ 20 deg
Performance	Load	$\tilde{q}\alpha$	$< 2.75 \cdot 10^5$
	Lateral	z $\dot{z}$	$<$ 167 m $<$ 15 m/s
	Actuation	δ_{pitch} Actuator usage should be minimized	$<$ 6.5 deg
	Tracking	TR1 (See above)	
	Disturbance Rejection	DR1 (See above)	

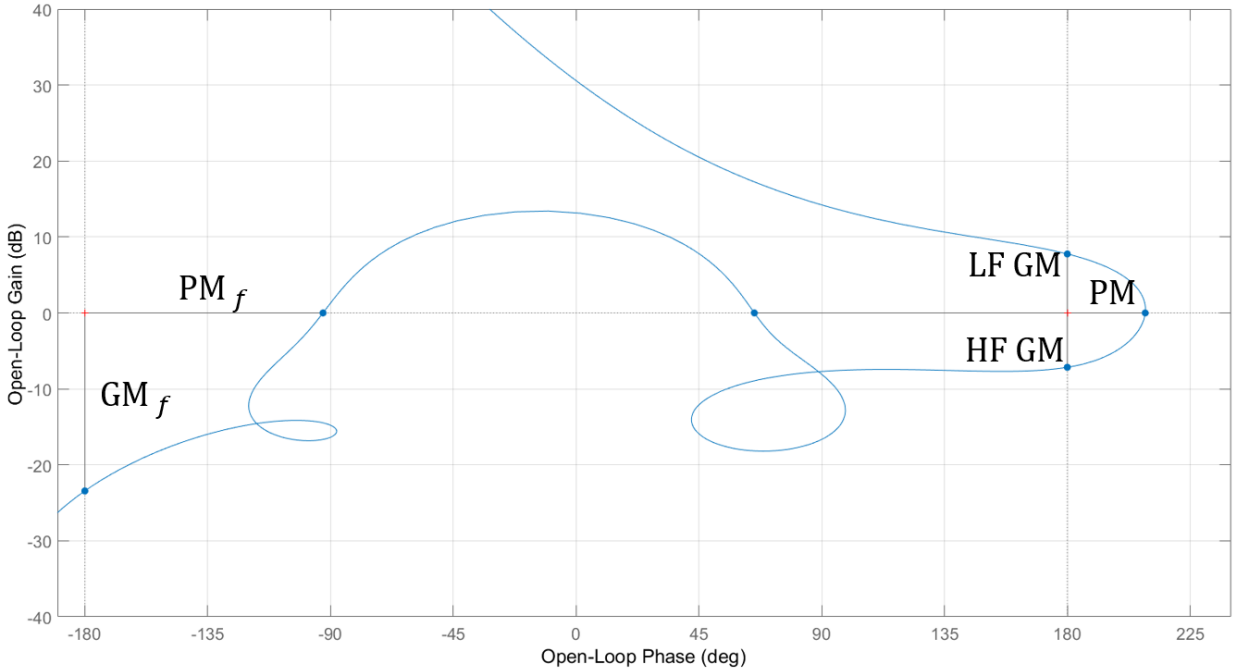

Fig. 2 Launch vehicle stability margins requirements.

Following [1], the controller is deemed to fulfill the stability requirements if the stability margins at the plant input meet the specified metrics. These metrics are most effectively visualized through a Nichols plot, as illustrated in Figure 2.

The performance requirements for the launch vehicle TVC system are divided into five categories. The first one, the load requirement, ensures that the loads applied to the LV remain below the maximum allowable value. This requirement is expressed as a function of $\tilde{q}\alpha$, which is hereafter referred to as the load performance metric (LPM). As seen in [1], the angle of attack is particularly sensitive to wind disturbances, highlighting the need for the control system to be robust against wind gusts in order to fulfill the load requirement.

Lateral requirements aim to bound the drift (z) and drift rate ($\dot{z}$) of the LV, which is especially critical due to the assumption that the LV employs open loop guidance. Actuation requirements, on the other hand, focus on limiting the maximum deflection angle (δ_{pitch}) and minimizing actuator usage. Tracking requirements ensure the controller can effectively track attitude commands while maintaining control over specific transient response parameters.

Finally, the controller must be capable of rejecting disturbances, with a primary emphasis on external disturbances such as wind gusts and bending modes.

III. $\mathcal{H}_\infty$ Open Loop Shaping - General Strategy

The $\mathcal{H}_\infty$ Open Loop Shaping design procedure originates from the early contributions of Vidyasagar (see for instance [10]). Subsequently, it was extensively detailed in [11], further refined in [12], [13], and in [14]. Finally, in [15] a systematic framework and practical application of the method is provided.

$\mathcal{H}_\infty$ Open Loop Shaping is a combination of an $\mathcal{H}_\infty$ optimization problem with classic open loop shaping methods. The open loop shaping methods aim at giving the open loop singular values the desired shape, while the $\mathcal{H}_\infty$ optimization aims at robustly stabilizing the shaped plant against normalized coprime factor (NCF) uncertainty.

The main advantages of this method stem from its ability to directly shape the open loop and robustify the system against NCF uncertainty, both of which address the challenges inherent to the $\mathcal{H}_\infty$ CLS method. Next, the steps required to apply $\mathcal{H}_\infty$ Open Loop Shaping will be outlined. The first step, explained in Subsection III.A, involves shaping the open loop singular values. The second step, covered in Subsection III.B, is the computation of the NCF robustifying controller. The third and final step, discussed in Subsection III.C, focuses on implementing the controller and the

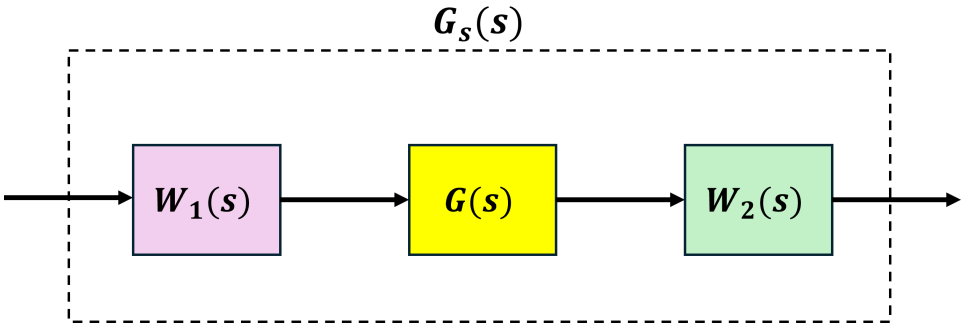

Fig. 3 Shaped plant.

weighting filters. This subsection will also provide guidance on how to integrate and apply each step within the overall design process.

A. Open Loop Shaping

The first step in the $\mathcal{H}_\infty$ Open Loop Shaping procedure is to shape the singular values of the open loop transfer functions ($L_O = GK$ and $L_I = KG$). This is done so as to achieve achieve the desired performance and robustness goals.

For the purpose of shaping the open loop transfer functions, two (generally diagonal) compensators are used: $W1$ and $W2$, which correspond to the pre-compensator and post-compensator, respectively. The full assembly, consisting of $W1(s)$, $W2(s)$, and $G(s)$, represents the shaped plant $G_s(s)$, as illustrated in Figure 3.

According to the guidelines established in [16], $W1$ is used to add integral action and reasonable roll-off rates for the open loop singular values, resulting in zero steady-state error while tracking commands, disturbance rejection and output decoupling. Additionally, proportional action can be added to $W1$ to decrease the phase-lag at crossover, resulting in higher stability. The choosing of the proportional gain, and therefore the PI's zero, results directly from the trade-off between bandwidth and robustness. Meanwhile, $W2$ is used for noise rejection (low-pass filter), and usually also contains lead-lag filters to adjust the crossover frequency, and reduce phase lag at crossover.

B. Robustifying Controller

The second step in $\mathcal{H}_\infty$ Open Loop Shaping is to compute a controller K which robustly stabilizes the shaped plant against normalized coprime factor uncertainty. Consider the shaped plant G_s, with a normalized left coprime

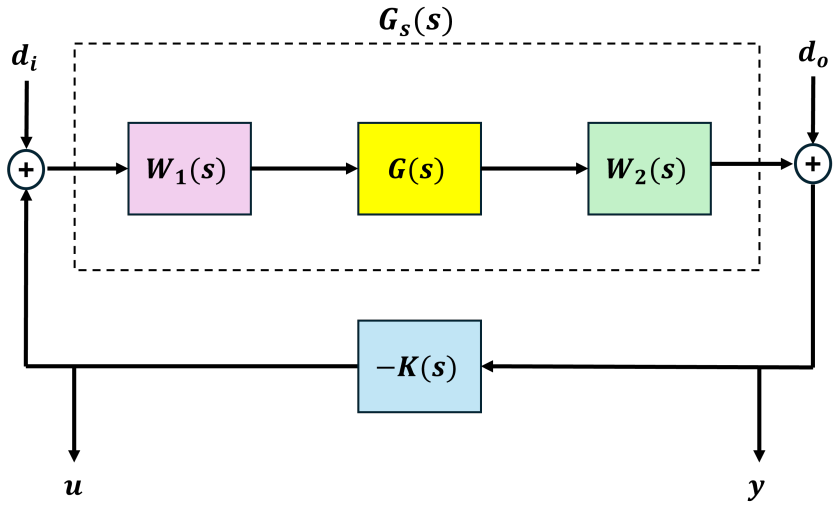

Fig. 4 NCF robustification scheme.

factorization $G_s = M^{-1}N$. An uncertain plant model can be written using the NCF specification as:

$$G_p = (M + \Delta_M)^{-1}(N + \Delta_N) \tag{12}$$

where the Δ's are stable and proper. The aim of the robust stabilization is to compute a controller which will robustly stabilize the class of perturbed plants defined by:

$$G_p = \left\{(M + \Delta_M)^{-1}(N + \Delta_N) : \|[\Delta_N \Delta_M]\|_\infty < \epsilon\right\} \tag{13}$$

The problem to be solved is to find the controller that maximizes (or nearly maximizes) the allowable coprime factor uncertainty (ϵ).

In [13] this problem is solved, and an analytical solution to compute a sub-optimal controller is found. This solution however, is only capable of generating full-order controllers. In this work, the controller used in the NCF robustification process will consist of four gains (a discussion on this is given later), therefore a full-order solution is not ideal.

In [15], it is shown that the process of finding a controller which maximizes ϵ is equivalent to finding a controller which minimizes the $\mathcal{H}_\infty$ norm of a specific four-block transfer function. So, combining that knowledge with systune, it is possible to compute a structured robustifying controller which maximizes the allowable coprime factor uncertainty. Figure 4 illustrates the diagram of the transfer function that must be minimized to compute the robustifying controller.

Finally, one useful mathematical formula is given. The greatest achievable robustness margin (γ_{min}) can be computed analytically through the following formula [15]:

$$\gamma_{min} = \epsilon_{max}^{-1} = \left\{1 - \left\|\begin{bmatrix} N & M \end{bmatrix}\right\|_H^2\right\}^{-\frac{1}{2}} \tag{14}$$

where $||.||_H$ is the Hankel norm. The Hankel norm of a system $G(s)$ is defined as [17]:

$$\|G(s)\|_H = \sqrt{\rho(PQ)} \tag{15}$$

where ρ is the spectral radius, P is the controllability Gramian and Q is the observability Gramian (the formulas for P and Q can be found in pages 133 and 136 of [17], respectively).

C. $\mathcal{H}_\infty$ Open Loop Shaping Design Process and Implementation

The process of applying $\mathcal{H}_\infty$ Open Loop Shaping consists of three steps. The first step involves shaping the open loop singular values, as described in Subsection III.A. However, this alone does not guarantee a robustly stable closed loop system.

The second step involves computing the robustifying controller to ensure closed loop robust stability. This step is divided into two sub-steps. The first sub-step involves using equation 14 to compute the maximum attainable stability margin. If $\gamma_{min} > 4$, the designer should revisit step one and adjust the weighting filters. If $\gamma_{min} < 4$, the loop shaping is considered successful, and the designer can proceed to the second sub-step. It is important to note that when $\gamma_{min} < 4$, implementing the robustifying controller will not significantly alter the shape of the open loop singular values (see [15]).

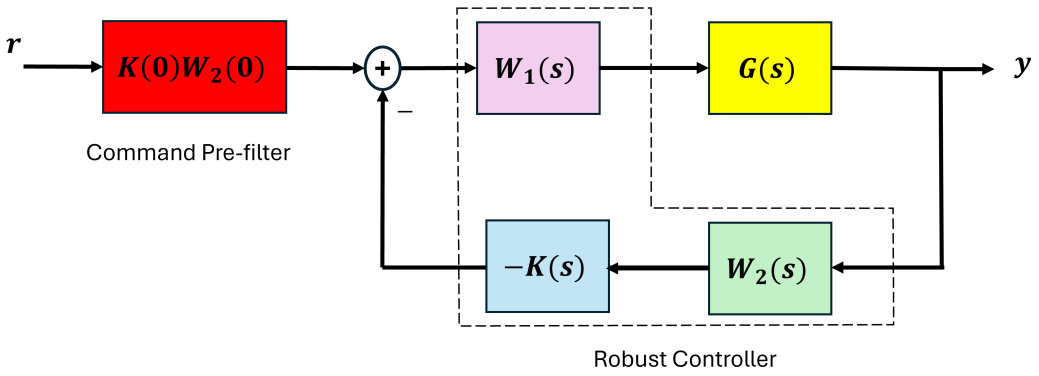

Fig. 5 $\mathcal{H}_\infty$ OLS tracker implementation.

Thus, robust stability is achieved without significantly degrading the performance characteristics specified by the open loop shaping.

The second sub-step involves designing the robustifying controller. This is accomplished by implementing the setup shown in figure 4 in SIMULINK and defining the controller $K(s)$ as a tunable parameter in systune. Then, $K(s)$ is computed by finding the stabilizing controller which minimizes the $\mathcal{H}_\infty$ norm of the transfer function pertaining the setup of figure 4.

The final step is to implement the $\mathcal{H}_\infty$ OLS robustifying controller and weighting filters. This can be achieved in various ways, including the regulator implementation, tracker implementation, and observer implementation. For this particular work, only a specific tracker implementation is relevant. The launch vehicle must be capable of tracking references, which makes the regulator implementation unsuitable. Additionally, the observer implementation would result in a controller of full order, which is impractical for this application. The tracker implementation in question is discussed in page 408 of [17], and is illustrated by Figure 5.

In the implementation of Figure 5, a command pre-filter is used to ensure zero steady-state tracking error, and the robust controller consists of the weighting filters and the NCF robustifying controller. It is important to note that this implementation avoids the direct excitation of the robustifying controller's dynamics by the reference commands, effectively preventing significant overshoot.

IV. $\mathcal{H}_\infty$ Open Loop Shaping - Application to Launch Vehicles

The application of $\mathcal{H}_\infty$ Open Loop Shaping (OLS) to aerospace vehicles is not always straightforward, as determining suitable weighting filters can be a cumbersome task. The first systematic application of $\mathcal{H}_\infty$ OLS to launch vehicles was presented in [6]. In this section, the weighting filter parametrization, as described in the referenced work, is reiterated for convenience, and a more detailed examination of the role of each weighting filter is provided, offering additional insight beyond previous treatments. A final note is given: in the following discussion the (often) mentioned desired loop shape, is the loop shape discussed and detailed in [6].

A. Weighting Filter Parametrization

The set of filters described in [6] follows the guidelines established by [16] for $\mathcal{H}_\infty$ Open Loop Shaping, which recommend placing proportional-integral action in the pre-compensator and lead-lag action in the post-compensator. The weighting filter parametrization is as follows:

$$\begin{aligned} W_1 &= Proportional - Integral \\ W_{2-z} &= Gain \\ W_{2-\dot{z}} &= Lead - Lag \\ W_{2-\theta} &= Gain \\ W_{2-\dot{\theta}} &= Lead - Lag \end{aligned} \tag{16}$$

As it can be seen, the pre-compensator is used to add proportional integral (PI) action on all channels. This is crucial as, in the LV case, all channels benefit from PI action (this will be further discussed later on). Moreover, this also ensures that the robust controller has a (desired) integrator-like shape. The post-compensator contains two gains: the drift gain is used to adjust the open loop singular values (SV) at low frequency (LF), whilst the pitch angle channel gain, is used to adjust the SV in the critical frequency (CF) range*. The two lead-lag (LL) filters in the post-compensator are used to delay the crossover and smoothen the curve around it.

In order to explain the effects and benefits of applying PI action on the pre-compensator, the reader must first understand the frequency dependency of the shaped plant's SV on each of the shaped plant's outputs. For that purpose, consider Figure 6, which compares the singular values of the open loop system, compensated with weighting filters according to the parametrization, to the singular values of the individual input-output channels of the same compensated system.

From the figure, it is evident that initially, the drift channel defines the open loop system response. As the frequency increases, the drift rate channel becomes dominant, until the effects of the non-minimum phase zero take place. Following this, the pitch channel takes over, and eventually the pitch rate becomes dominant for the rest of the frequency

*Frequency range identified in [6] to be most relevant for load relief.

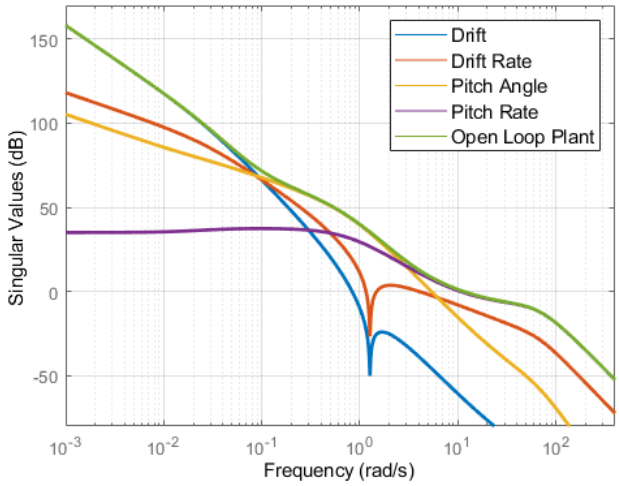

Fig. 6 SV of compensated open loop vs SV of compensated individual input-output channels.

domain. It should be noted, that after the transition from pitch to pitch rate, and up until shortly after crossover, the drift rate channel has an influence on the response.

Having understood that each output channel is dominant at a certain frequency range, it is now possible to discuss the importance of the PI pre-compensator. Additionally, the role of the LL filters will also be discussed.

Consider Figure 7, which shows the singular value plots of the weighted system's individual input-output channels. Each subplot presents singular values for a specific input-output pair, illustrating the effect of progressively applied filter sets:

- Blue: SVs of the plant shaped with only static gains.
- Red: SVs of the shaped plant when a PI controller is included in the pre-compensator, and static gains are kept equal to those of the blue curve.
- Yellow: SVs of the shaped plant when a PI controller is included in the pre-compensator, lead-lag filters are added to the output rate channels, and static gains are kept equal to those of the blue curve.

This layered approach — from gains only, to PI control, to the full parametrization — highlights the frequency response modifications introduced by each filter set across the different input-output channels. It is now easier to look at each individual channel and explain the contributions of the weighting filters.

Adding integral action to the drift channel ensures a high low frequency gain and a steeper roll-off at low frequencies. As this output is dominant at low frequencies, the integral action guarantees that the open loop response achieves the desired shape in this frequency range.

Adding integral action to the drift rate channel achieves the same results as the drift channel. Moreover, it ensures that the open loop gain maintains an integrator-like shape as the drift rate channel becomes dominant. Additionally, the integral action decreases the gain after the non-minimum phase zero, which is beneficial, as it allows to further increase drift rate gain without delaying the crossover. This adjustment results in improved load relief while maintaining actuation levels, as the increased drift rate gain raises the open loop singular value in the critical frequency range.

In the pitch channel, adding integral action results in a steep SV slope, allowing for an increase of the pitch channel gain, whilst maintaining crossover. Once again, enabling better load relief.

Adding integral action to the pitch rate channel results in a steeper SV slope, enabling an increase in gain while maintaining the crossover frequency. While this does not directly contribute to load relief, it facilitates a smoother transition from the pitch-dominated region to the pitch rate-dominated region.

The role of the PI in the pitch and pitch rate channel is particularly important due to the non-minimum phase (NMP) zero in the drift rate channel. The NMP zero causes a sudden decrease in the open loop SV at a frequency critical for load relief. This could only be solved through an increase in pitch/pitch rate output channel gains, as these are the channels active in the relevant frequency range. Without the integral action, the increase in gain would cause a tremendous increase in crossover frequency, leading to unacceptable actuation levels.

Finally, the lead-lag action allows for the adjustment of both crossovers in the output rate channels. As shown in Figure 6, these are the dominant channels near the crossover. Testing has shown that both lead-lag filters are necessary to achieve the desired open loop specifications. It should be noted, that the lead lags are only required, due to the low

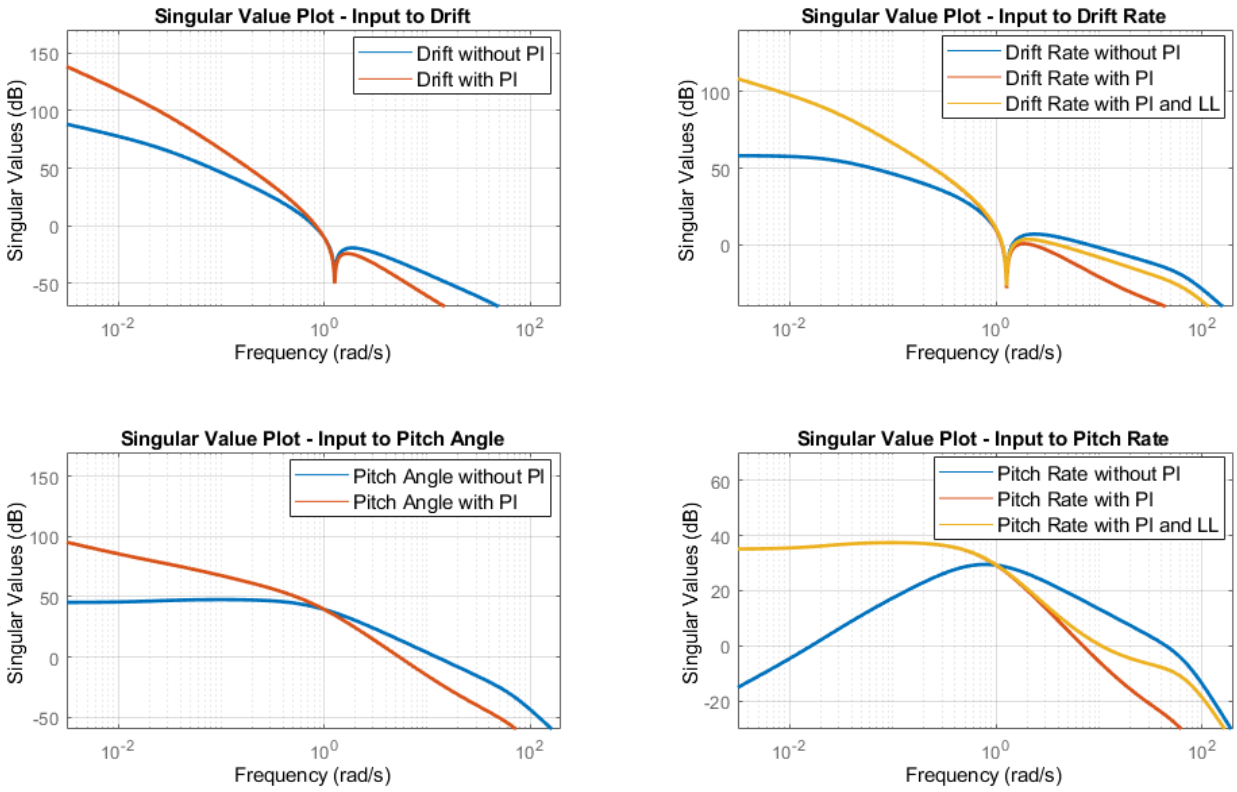

Fig. 7 PI filter and LL filter effect on the individual channels.

order of the robustifying controller in this work (only four gains). In essence, the lead lags are aiding the robustifying controller in performing the NCF robustification.

V. $\mathcal{H}_\infty$ Closed Loop Shaping vs $\mathcal{H}_\infty$ Open Loop Shaping

As discussed in [6], preliminary results indicated that $\mathcal{H}_\infty$ OLS and $\mathcal{H}_\infty$ CLS yield identical controllers for launch vehicles. This result is further confirmed through two examples presented in Subsection V.A. An important remark must be made: the analysis of these examples relies on the insights provided in [6] regarding the most relevant frequency ranges for each LV performance objective, as well as the correspondence between performance goals and open-loop specifications. Readers unfamiliar with these concepts are encouraged to consult Section 4 of the aforementioned work.

A. $\mathcal{H}_\infty$ CLS vs $\mathcal{H}_\infty$ OLS - Examples

In [6] it was shown that $\mathcal{H}_\infty$ CLS could be used to reproduce the controller produced with $\mathcal{H}_\infty$ OLS. For this purpose, six closed loop constraints were utilized: one to limit the allowable load, one to limit the allowable drift motion, one to limit the allowable TVC deflection, one to limit the peak SV of the pitch angle's sensitivity transfer function, one to shape the maximum SV of the plant's input sensitivity transfer function and one to enforce minimum input stability margins. The produced controllers consisted of five weighting filters (as parametrized in Subsection IV.A) and two Proportional-Derivative controllers applied on pitch angle and drift[†] (consider Figure VI.A to visualize the control implementation scheme, for the case where a flexible LV is considered). Using the same controller order and structure, the same closed loop constraints (retuned), and considering only rigid-body dynamics (i.e., neglecting bending mode contributions from the model in Section II), two examples are presented to illustrate that $\mathcal{H}_\infty$ CLS cannot outperform $\mathcal{H}_\infty$ OLS.

In the first example, the goal was to improve load relief and drift rejection. This was achieved through tightening

[†]These act as the robustifying controller for the $\mathcal{H}_\infty$ OLS controllers.

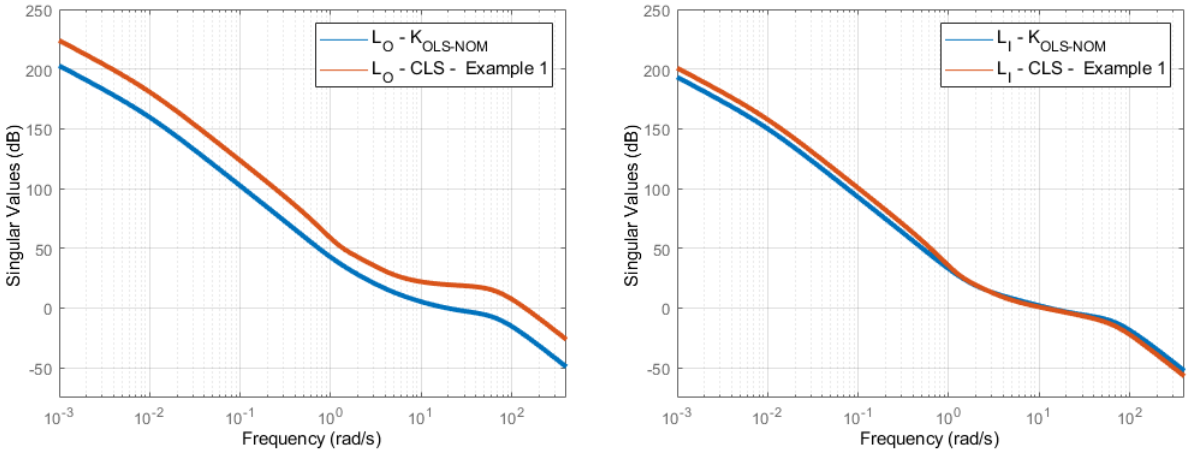

Fig. 8 Output open loop (on the left) and input open loop (on the right) SV comparison - $K_{OLS-NOM}$ vs 1st improvement attempt with $\mathcal{H}_\infty$ CLS.

the load and the drift constraints and loosening the pitch angle sensitivity and actuation constraints. Note that the constraints had to be loosened so as to ensure that all optimization constraints were complied with. In Figure 8, the L_I and L_O of the resulting controller are compared to those of $\mathcal{H}_\infty$ OLS controller (coined $K_{OLS-NOM}$). As it can be seen, not only the load relief and the drift/drift rate rejection were improved, but the L_I shape was also improved: the new controller has essentially the same L_I crossover, with higher L_I SV prior to crossover and slightly lower L_I SV post crossover. However, these improvements come at the cost of a significantly later crossover in the L_O SV plot, as well as much higher L_O SVs at higher frequencies. This results in a controller with worse robustness to output multiplicative uncertainty, as well as worse noise attenuation.

In the second example, the goal was, again, to improve load relief, drift rejection, whilst maintaining high frequency L_O gain low. This was achieved through tightening the load and drift constraints, loosening the sensitivity and actuation constraints, and replacing the constraint applied to the plants input sensitivity transfer function with a constraint limiting the $\mathcal{H}_\infty$ norm of the transfer function from the noise input to all of the outputs. In Figure 9, the L_I and L_O of the new controller are compared to those of nominal $\mathcal{H}_\infty$ OLS controller. As shown, the new controller demonstrates a clear improvement in the L_O shape. Its L_O achieves the same crossover frequency as the L_O of the $\mathcal{H}_\infty$ OLS controller, but displays equal or higher gain at frequencies prior crossover and essentially the same gain afterward. However, the L_I transfer function of the new controller exhibits significantly lower gain at low frequencies, while maintaining comparable gain to $K_{OLS-NOM}$ around and beyond the crossover frequency. Overall, the new controller has improved

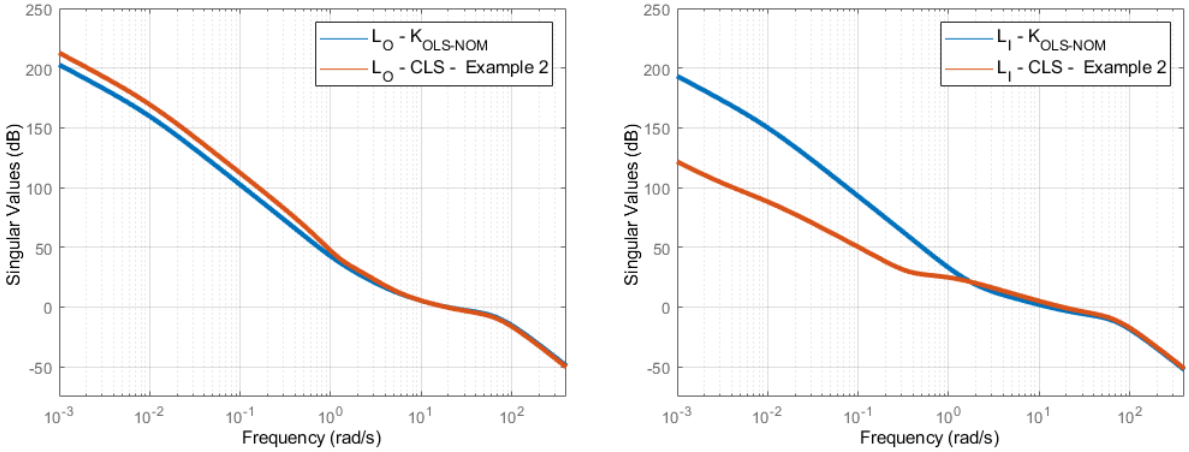

Fig. 9 Output open loop (on the left) and input open loop (on the right) SV comparison - $K_{OLS-NOM}$ vs 2nd improvement attempt with $\mathcal{H}_\infty$ CLS.

load relief and drift/rate rejection, but reduced attenuation of input disturbances at the plant input.

Both examples help to convey that any improvement in the loop gain of the $\mathcal{H}_\infty$ OLS controller is always offset with worsening of the loop gain somewhere else. This is further evidenced by the fact that to tighten any closed loop constraint, other closed loop constraints need to be loosened. These results further confirm the findings of [6] and support the conclusion that $\mathcal{H}_\infty$ Closed Loop Shaping and $\mathcal{H}_\infty$ Open Loop Shaping can yield (almost) identical controllers, with neither method offering a clear performance advantage over the other. However, as discussed in [6], the complexity involved in applying each method differs significantly. $\mathcal{H}_\infty$ OLS reduces the number of transfer functions that require shaping, automatically ensures robustness at both the plant input and output, and offers greater reproducibility across different flight points. These advantages—combined with the observation that $\mathcal{H}_\infty$ CLS and $\mathcal{H}_\infty$ OLS produce similar results—make a compelling case for preferring $\mathcal{H}_\infty$ OLS in the design of launch vehicle attitude controllers.

VI. $\mathcal{H}_\infty$ Open Loop Shaping for Flexible Launch Vehicles

In the traditional approach to TVC control, the design of the rigid body controller and the bending filter for the flexible modes is treated separately. The design process has three steps: firstly, the rigid body controller is designed; secondly, the flexible interactions are added to the model and the bending filter is tuned; thirdly, the rigid body controller and bending filter are manually re-tuned to ensure proper integration and compliance with all requirements.

As described in [1], efforts have been made to streamline this process. In particular, [1] developed and implemented a method that allows for the simultaneous design of both the rigid body controller and the bending filter using $\mathcal{H}_\infty$ Closed Loop Shaping. Building on this concept, the current work will develop an integrated approach for designing the Rigid/Flexible body controller using the $\mathcal{H}_\infty$ Open Loop Shaping method.

And so, this section is structured as follows: Subsection VI.A covers the parametrization and implementation of the bending filter; Subsection VI.B presents the rigid controller and bending filter design using the separate design approach; Subsection VI.C describes and implements the integrated design approach; Subsection VI.D compares the results from both approaches; Subsection VI.E combines the multi-model approach and the integrated approach to produce a robustly tuned controller; Subsection VI.F shows selected time and frequency-domain simulation results of the two $\mathcal{H}_\infty$ OLS integrated controllers. It should be noted that both for the separate and integrated approaches, the loop shaping filters are chosen using the guidelines and insight given in [6].

A. Bending Filter Parametrization and Implementation

For this work, the bending filter parametrization that will be used is the one outlined in [1]. This parametrization, which is detailed in eq. 17, was developed to enable the application of structured $\mathcal{H}_\infty$ design, while preserving the legacy knowledge of the original bending filter used by the VEGA GNC team.

$$H_{BF}(s) = \prod_{i=1}^{4} \frac{s^2 + \eta_i s + (\omega_i)^2}{s^2 + \eta_i/\epsilon_i s + (\omega_i)^2} \cdot \left(\frac{\epsilon_{LP} s^2 + \eta_{LP} s + \left(0.6\omega_{q_2}\right)^2}{s^2 + \eta_{LP} s + \left(0.6\omega_{q_2}\right)^2} \right)^3 \tag{17}$$

This bending filter consists of four notch filters and a low-pass filter. The notch filters are centered around the minimum expected frequency of the 1st bending mode (BM), the nominal frequency of the 1st BM, the maximum expected frequency of the 1st BM and the minimum expected frequency of the 2nd BM, respectively. These filters aim at notching the first and second BM, whilst the low-pass filter aims at attenuating the upper BMs.

Table 2 Fixed and tunable Variables of the bending filter parametrization.

Fixed Variables		Tunable Variables		
Variable	Value	Variable	Min	Max
ζ_1	2	ϵ_1	−25 dB	−10 dB
ζ_2	5	ϵ_2	−10 dB	−4 dB
ζ_3	2	ϵ_3	−25 dB	−10 dB
ζ_4	12	ϵ_4	−20 dB	−15 dB
η_{LP}	40			
ϵ_{LP}	−8.3 dB			

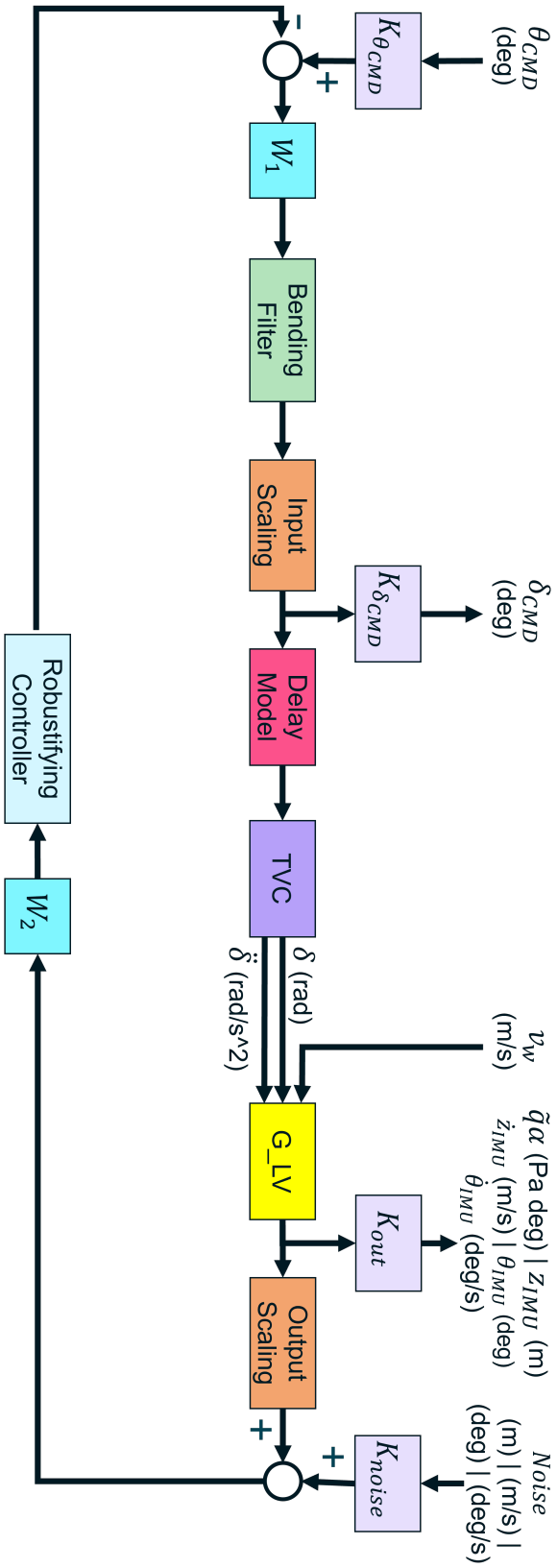

Fig. 10 Tracker implementation scheme for the rigid/flexible body $\mathcal{H}_\infty$ OLS controllers.

Each notch filter is parameterized by two variables, ϵ_i and η_i. The first parameter is tunable and corresponds to the attenuation at the center frequency of the notch filter, while the second is fixed and describes the width of the filter. The low-pass filter is fixed as well, with ϵ_{LP} representing the attenuation at high frequencies, and η_{LP} being defined as in eq. 18.

$$\eta_{LP} = 2\,\zeta\,(0.6\,\omega_{q_2}) \tag{18}$$

where ζ is the low pass filter's damping factor, and ω_{q_2} is the nominal frequency of the second BM.

In this work, both the fixed and tunable variables are set according to the values and limits specified in [1]. These can be seen in Table 2. With this in mind, the implementation of the bending filter can be seen in Figure 10. In this scheme the output gains convert signals from radians to degrees, while the input gains convert signals from degrees to radians. The one exception is the command input gain, which has two functions: to convert degrees to radians, and to act as the prefilter. Finally, the plant input/output scaling was defined according to the guidelines described in [17].

B. Separate Rigid/Flexible Body Controller Design

The goal of the separate rigid/flexible body controller design is to serve as baseline for the comparison. In this step, the rigid body controller will still be designed with $\mathcal{H}_\infty$ Open Loop Shaping, whilst the bending filter is tuned by hand. In addition to ensuring that the final controller meets all the requirements defined in Subsection II.D, another key objective is to ensure that the 1st BM peak gain in the input open loop gain was similar to that of the controller developed in [1]. Achieving the latter condition is expected to ensure proper damping of the 1st BM, as the strong performance of this reference controller has already been validated through nonlinear simulation.

Figure 11 illustrates the design process for the separate rigid/flexible body controller. This process is divided into three main phases: initial, intermediate, and final. Several important remarks need to be made regarding each phase.

In the first step of the initial phase, a loose rigid body shape was employed (i.e., $W_{2-\theta} = 0.01$, $W_{2-z} = 0.01$, $W_1 = 4\left(\frac{s+11.5}{s}\right)$), as experimental observations revealed that the introduction of the bending filter required lower loop gain specifications to achieve a sufficiently large robustness margin. It should be noted that for the first step of the initial phase, only rigid body behavior was considered.

In the second step of the initial phase, the bending filter was incorporated, with the ϵ_i parameter of each notch filter initially set to the midpoint of its allowable range. For this step and all subsequent steps, the flexible behavior of the LV was taken into account.

In the intermediate phase, fine-tuning the bending filter to achieve the desired flexible stability margins and 1st BM peak gain involved minor trial and error. The condition $\gamma \leq 4$ was applied to ensure that the lead-lags were appropriately selected, minimizing the need for significant adjustments in the final phase.

In the final phase, selecting the bending filter and determining the drift and pitch angle post-compensator gains ($W_{2-\theta}$ and W_{2-z}) proved to be a non-trivial task, requiring extensive experimentation. Adjusting the drift and pitch angle post-compensator gains impacted the loop gain at the 1st BM frequencies, creating the need for additional notching at those frequencies. This adjustment process was particularly challenging, as excessive notching led to an overly steep slope near the crossover frequency. Moreover, finding the optimal combination of drift and pitch angle post-compensator gains added complexity, as multiple configurations were possible.

Through testing various controllers, it was concluded that the drift post-compensator gain should be set to 0.21, and the pitch angle post-compensator gain increased as much as possible, while maintaining $\gamma \leq 4$. This drift post-compensator gain is the smallest which allowed for sufficient drift rejection (as demonstrated by Monte Carlo time domain simulations). Therefore, by selecting this drift post-compensator gain and increasing pitch angle post-compensator gain as much as possible, while maintaining $\gamma \leq 4$, it will be possible to maximize load relief while attaining sufficient drift rejection (according to the considerations given in [6]). With this in mind, extensive trial and error was carried out, and the final bending filter configuration was determined: ϵ_2 and ϵ_4 were set to their minimum values, while ϵ_1 and ϵ_3 were adjusted to -21.3 dB and -11.9 dB, respectively. This configuration was selected because it supported the chosen drift post-compensator gain, and allowed for the highest possible pitch angle post-compensator gain, while ensuring that the 1st BM peak gain and the nominal flexible stability margins were as desired.

Finally, one important remark is made regarding the rationale of maintaining $\gamma \leq 4$. From the rigid body design performed both in this work and in [6], it was known that stability requirements for the LV were generally easy to meet, while the load relief and drift rejection requirements were the most likely to be infringed. Moreover, using the $\mathcal{H}_\infty$ OLS methodology described in [6] and targeting a robustness margin smaller or equal to four typically resulted in fulfilling the LV stability margins requirements. Testing showed this to be true for the rigid/flexible body controller design as well. Therefore, by ensuring the robustness margin remained below four and maximizing the drift and pitch

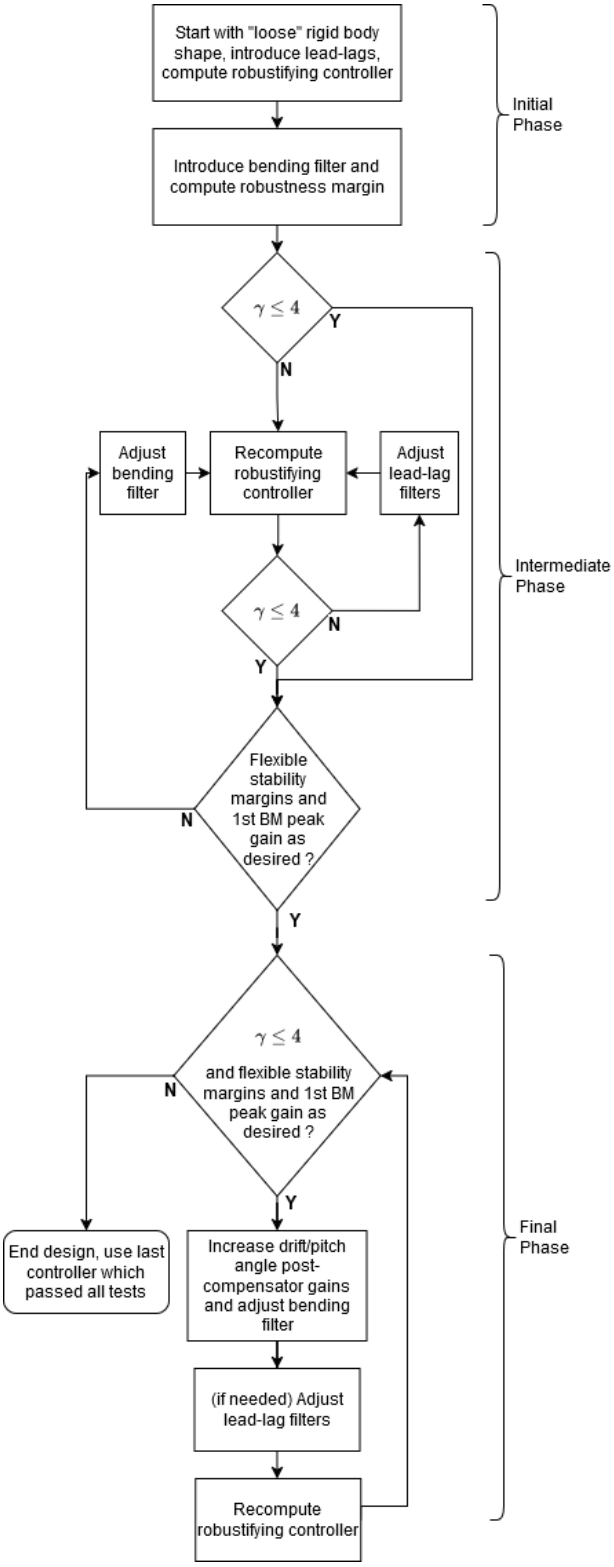

Fig. 11 Workflow of the separate rigid/flexible body controller design.

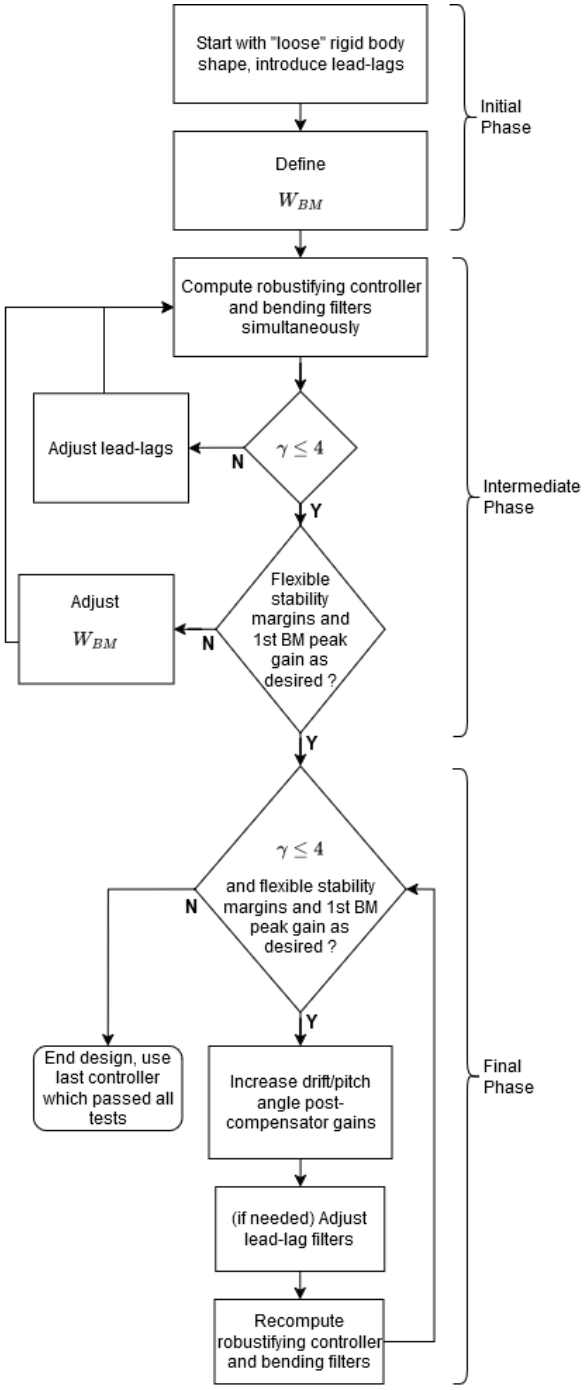

Fig. 12 Workflow of the integrated rigid/flexible body controller design.

angle post-compensator gains (which are directly related to improving drift and load rejection as discussed in [6]) it was possible to achieve a controller with sufficiently large stability margins and optimal load/drift rejection. This controller is coined $K_{OLS-NOM-SEP}$ and will be shown in Subsection VI.D. However, before that, the integrated design approach will be discussed in the following subsection.

C. Integrated Rigid/Flexible Body Nominal Design

This section discusses a process for designing an integrated rigid/flexible body controller, with the primary goal of simultaneously tuning the robustifying controller and bending filter.

For all steps, the LV is considered to have unneglectable flexible behavior. Furthermore, to achieve the simultaneous tuning of the robustifying controller and bending filter, two optimization objectives are employed during the use of systune: NCF robustification and maximum allowable loop gain. The last objective is only applied at bending mode frequencies and is formally defined in eq. 19.

$$\bar{\sigma}(L_I(\omega)) < W_{BM}, \quad \forall \omega \in \omega_R \tag{19}$$

where W_{BM} is a static filter and where ω_R is a frequency range spanning from 20 rad/s (slightly before the first BM), to infinity. It should be noted that this constraint was applied on L_I, as the requirement for the 1st BM peak gain pertains to the input open loop gain.

The step-by-step procedure for designing the integrated controller is detailed in Figure 12. As it can be seen, there are once again three phases (initial, intermediate and final) during the design. Some important remarks regarding the intermediate and final design phases are given next.

In the intermediate design phase, the goal is to select the static filter (W_{BM}) used for the maximum allowable loop gain constraint. If done properly (i.e. fulfilling the conditions given in the workflow of Figure 12), the flexible stability margins and 1st BM peak gain will be as desired during the rest of the design. Subsequently, the designer can move on to the final phase, and focus solely on optimizing the performance of the controller.

In the final phase, the drift post-compensator gain was set to 0.21, as testing showed it to be the minimum drift post-compensator gain that provided adequate drift rejection (as found in Monte Carlo time domain simulations). Subsequently, pitch post-compensator gain was increased as much as possible, while maintaining $\gamma < 4$, for the same reasons as in the separate design.

Finally, it is important to mention that it is possible to tune the lead-lag filters simultaneously with the bending filter and robustifying controller. To do so, in the intermediate and final phase of the integrated design, the designer must set the lead-lags, bending filters and robustifying controller as tunable parameters in systune. Subsequently, all of them can be computed simultaneously, utilizing as optimization goals the NCF robustification and the aforementioned maximum allowable loop gain. Care should be taken when opting for this design approach, as the lead-lags must be properly parametrized and constrained.

With the integrated approach it was possible to design a rigid body controller and bending filter in a much simpler way than with the separate approach. In fact, it should be noted that the application of the integrated design methodology took far less time than the separate design methodology. This is mainly a result of the simultaneous robustifying controller/bending filter tuning, which not only eliminates the need for manual bending filter adjustments, but also enables a smoother and automatic integration of the two components. The controller computed with this method is coined $K_{OLS-NOM-INT}$ and will be shown in the next subsection.

D. Comparison of the Results

First, both the computed rigid body controllers and bending filters are presented in Table 3. As shown, all the filters and robustifying controllers are quite similar. However, several key observations should be made.

In both designs, the pre-compensator was initialized with the same value and remained unchanged throughout the process. Additionally, the drift post-compensator gains were selected based on testing controllers produced by each respective approach, ensuring they did not influence the choice of one another. The pitch angle post-compensator gains were maximized independently for each design, with no interaction between them, as the objective was to achieve the highest possible gains in each approach.

Furthermore, although the lead-lag compensators were manually tuned in both approaches — potentially raising concerns that the results of the integrated design were influenced by the separate design — testing in the integrated design confirmed that they were the optimal choice for fulfilling the tuning requirements. Notably, when the lead-lags were simultaneously tuned with the bending filter and robustifying controller in the integrated approach, they naturally

Table 3 Robustifying controller, bending filter and weighting filters comparison - $K_{OLS-NOM-SEP}$ vs $K_{OLS-NOM-INT}$.

	$K_{OLS-NOM-SEP}$	$K_{OLS-NOM-INT}$
W_1	$\frac{4(s+11.5)}{s}$	$\frac{4(s+11.5)}{s}$
W_{2-z}	0.21	0.21
$W_{2-\dot{z}}$	$\frac{30(s+0.23)}{(s+14.49)}$	$\frac{30(s+0.24)}{(s+14.95)}$
$W_{2-\theta}$	0.12	0.12
$W_{2-\dot{\theta}}$	$\frac{0.21(s+1.92)}{(s+10.07)}$	$\frac{0.21(s+1.91)}{(s+10.08)}$
K_{p_θ}	−0.2928	−0.3007
K_{d_θ}	−1.1526	−1.1532
K_{p_z}	0.4253	0.4255
K_{d_z}	0.5451	0.5422
ϵ_1	−21.3	−21.3407
ϵ_2	−10	−10
ϵ_3	−11.9	−11.9035
ϵ_4	−20	−20

converged to nearly the same values as those determined during the manual tuning. This convergence highlights that their selection and tuning were driven by the design objectives, rather than by any prior knowledge from the separate design process. With this discussion in mind, it becomes clear that the experience from the first design did not influence the second design.

Despite the differences in design approach, both methods produced nearly identical results. Figure 13 highlights this by comparing the open loop gains of the two controllers, which are shown to be identical. Furthermore, Figure 14 presents two comparisons: the first compares the input Nichols plots of each controller, while the second compares the Bode plots of the bending filters of each controller. Both comparisons show indistinguishable results, further validating the consistency of the design approaches.

In essence, both methods yield the same results, which is a crucial finding given that the integrated design method is significantly simpler and faster to implement.

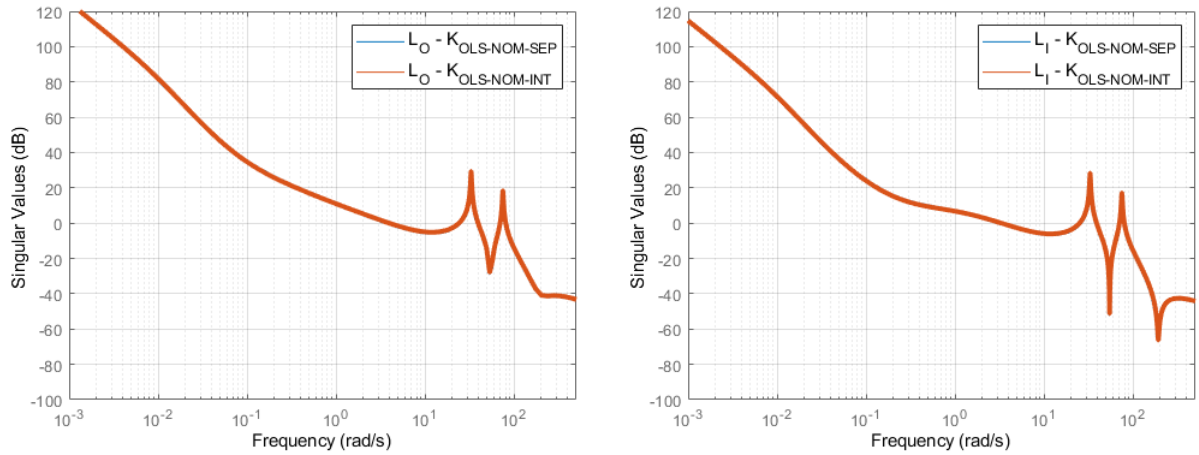

Fig. 13 Output and input open loop (L_O on the left and L_I on the right) SV comparison - $K_{OLS-NOM-SEP}$ vs $K_{OLS-NOM-INT}$.

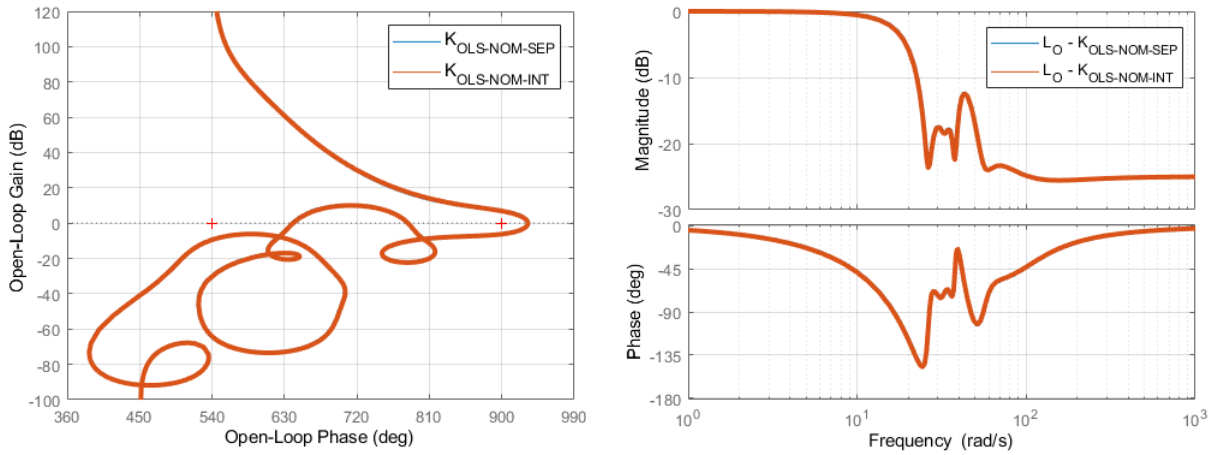

Fig. 14 Input Nichols plot (on the left) and Bode plot of the bending filters (on the right) - $K_{OLS-NOM-SEP}$ **vs** $K_{OLS-NOM-INT}$**.**

E. Integrated Rigid/Flexible Body Multi-model Controller Design

The objective of the Multi-model design approach was to ensure that the bending filter and rigid body controller were robustly tuned, meeting stability and performance requirements even under uncertainty. To accomplish this, the design process accounted for both the nominal model and the corner cases defined by five uncertain parameters. These parameters included the frequencies of the first two bending modes, as well as the three rigid body parameters with the highest mu-sensitivity (for a description of this concept see [18]): Cn_α, $\tilde{q}$ and x_{cp}.

After defining the models to be used for the design, the integrated rigid/flexible body controller design approach was applied, resulting in the controller labeled $K_{OLS-MM5-INT}$. The weighting filters, robustifying controller, and bending filter of $K_{OLS-MM5-INT}$ are compared with those of $K_{OLS-NOM-INT}$ in Table 4.

It should be noted that, for the Multi-model design, the pre-compensator and lead-lags were adjusted to ensure $\gamma = 4$. The drift post-compensator gain was set equal to that of the nominal integrated controller, as testing has shown this ensures sufficient drift rejection. Additionally, the pitch angle post-compensator gain was slightly reduced compared to

Table 4 Robustifying controller, bending filter and weighting filters comparison - $K_{OLS-MM5-INT}$ **vs** $K_{OLS-NOM-INT}$**.**

	$K_{OLS-MM5-INT}$	$K_{OLS-NOM-INT}$
W_1	$\frac{6.26(s+10.2)}{s}$	$\frac{4(s+11.5)}{s}$
W_{2-z}	0.21	0.21
$W_{2-\dot{z}}$	$\frac{30(s+0.30)}{(s+19.09)}$	$\frac{30(s+0.24)}{(s+14.95)}$
$W_{2-\theta}$	0.1	0.12
$W_{2-\dot{\theta}}$	$\frac{0.12(s+1.8)}{(s+5.78)}$	$\frac{0.21(s+1.91)}{(s+10.08)}$
K_{p_θ}	−0.3000	−0.3007
K_{d_θ}	−0.9864	−1.1532
K_{p_z}	0.3441	0.4255
K_{d_z}	0.4556	0.5422
ϵ_1	−16.52	−21.3407
ϵ_2	−10	−10
ϵ_3	−10	−11.9035
ϵ_4	−17.91	−20

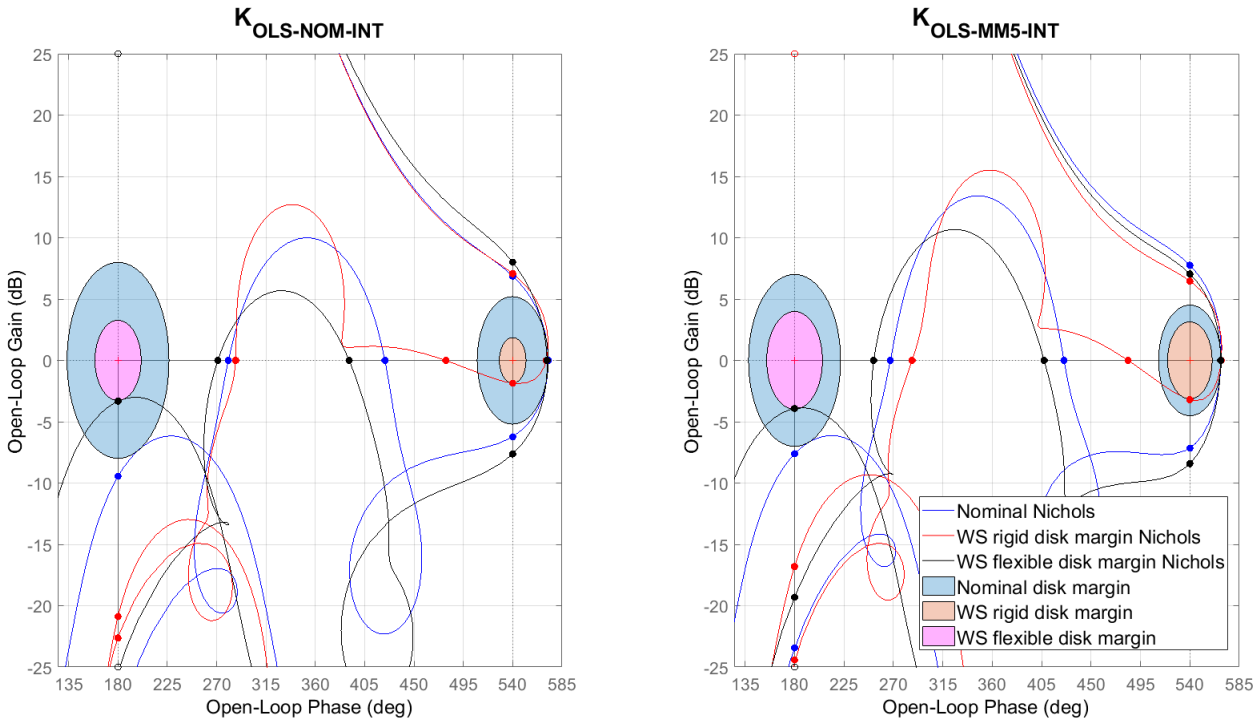

Fig. 15 Input Nichols - $K_{OLS-NOM-INT}$ vs $K_{OLS-MM5-INT}$.

the nominal controller in order to satisfy the desired stability margin requirements.

F. Results

In the following analysis, dispersed condition testing refers to results obtained from 1000 Monte Carlo simulations. Two specific tests are presented: input stability margins, which illustrate the controller's robust stability; and time-domain simulation of a low frequency, high amplitude (higher than the maximum expected) wind gust applied to the LV, to showcase robust performance.

1. Input Stability Margins

The input Nichols plot (Figure 15) contains three lines, one representing the nominal Nichols (blue line), one representing the Nichols corresponding to the worst-sampled rigid disk margin (red line), one representing the Nichols corresponding to the worst-sampled (WS) flexible disk margin (black line). The blue disks represents the nominal disk margins, while the red and purple disks represent the worst-sampled rigid/flexible disk margins, respectively. The worst-sampled disk margins are the regions in which, according to the testing, the Nichols plot is not expected to enter.

As shown in Figure 15, the nominal controller exhibits good nominal rigid and flexible margins, as well as strong worst-sampled case flexible margins. However, its rigid margins in the worst-sampled cases are smaller and unacceptable according to the requirements (smaller than 3 dB and 20 deg). In contrast, the Multi-model controller has slightly smaller nominal margins, but significantly larger rigid and flexible margins in the worst-sampled cases. In fact, while both controllers meet the stability requirements for nominal rigid and flexible margins as well as dispersed flexible margins, only $K_{OLS-MM5-INT}$ achieves sufficient rigid margins under dispersed conditions.

Fig. 16 Color code for time domain analysis - $K_{OLS-NOM-INT}$ vs $K_{OLS-MM5-INT}$.

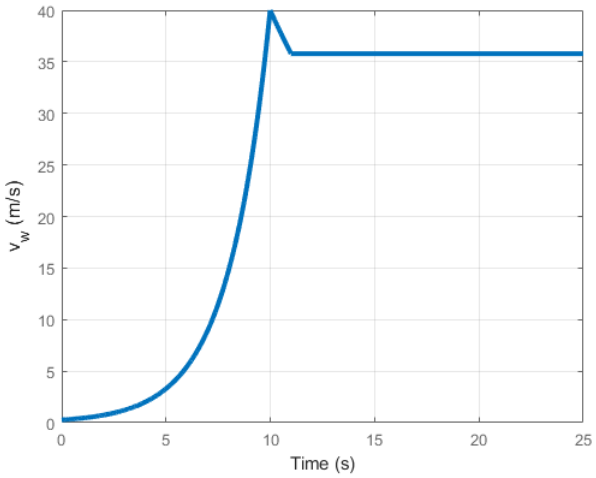

Fig. 17 Wind gust input signal for LFHA simulation.

2. Time Domain Analysis

The following figures show the time-domain simulation results of relevant LV quantities when the vehicle is subjected to a low frequency high amplitude (LFHA) wind gust. The wind input signal is shown in Figure 17[‡]. The color coding for the integrated controllers corresponds to the scheme defined in Figure 16. Additionally, shaded regions in the plots indicate the range of outcomes under dispersed conditions.

In terms of load performance metric (LPM), drift, and drift rate (Figures 18, 19, and 20, respectively), both controllers exhibit very similar responses under nominal and dispersed conditions, with the nominal controller showing a slight advantage. This difference can be attributed to the multi-model controller's marginally improved pitch angle performance in both nominal and dispersed conditions (see Figure 21). The Multi-model controller also exhibits a smaller pitch rate peak value, as illustrated in Figure 22, and nearly indistinguishable nominal and dispersed conditions results in actuation, as shown in Figure 23.

Overall, all plots demonstrate results well within the performance requirements for nominal and dispersed conditions: drift rate remains below one-third of its requirement, drift stays under one-fifth, the load performance metric (LPM) remains below 80% of its limit, and TVC deflection remains below one-third of its allowable value.

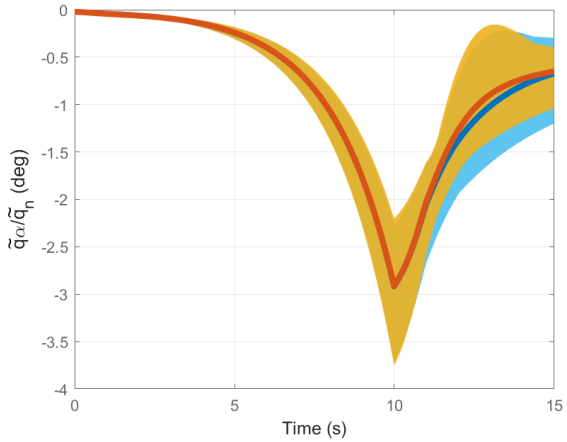

Fig. 18 LFHA Wind - Load performance metric (LPM), normalized by the nominal dynamic pressure.

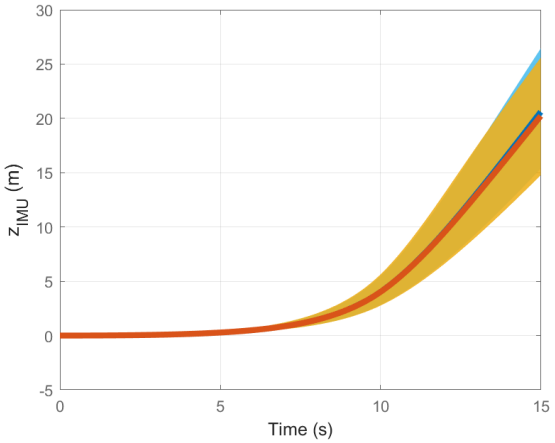

Fig. 19 LFHA Wind - Drift.

[‡]This wind input signal follows a commonly used shape for LV testing, as discussed in [7].

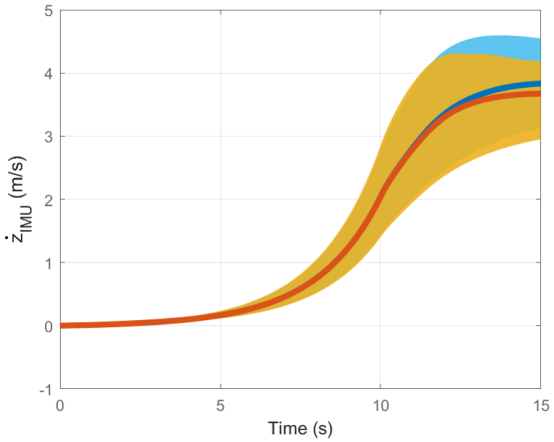

Fig. 20 LFHA Wind - Drift rate.

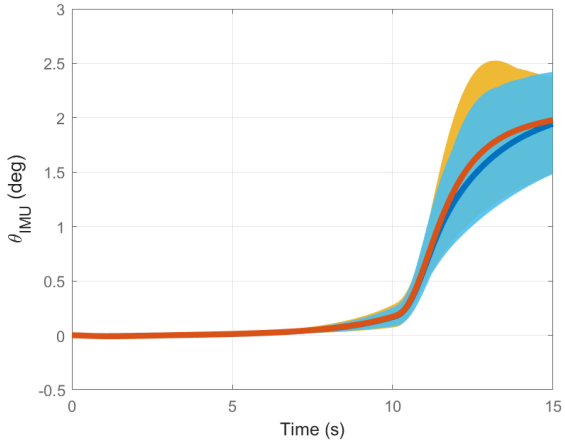

Fig. 21 LFHA Wind - Pitch angle.

VII. Conclusion

In this work, the use of $\mathcal{H}_\infty$ Open Loop Shaping (OLS) for the design of launch vehicle (LV) thrust vector control (TVC) systems has been further investigated and extended. Building upon previous work [6], where $\mathcal{H}_\infty$ OLS was proposed as a simpler and more systematic alternative to $\mathcal{H}_\infty$ Closed Loop Shaping (CLS), this paper has provided additional insights into the weighting filter parametrization and expanded the comparison between both approaches. Through two rigid-body examples, it was shown that $\mathcal{H}_\infty$ OLS and $\mathcal{H}_\infty$ CLS result in nearly identical controllers, with neither method offering a performance advantage over the other. However, the reduced complexity and improved reproducibility of $\mathcal{H}_\infty$ OLS across flight points, make it a more practical choice for LV control system design.

The $\mathcal{H}_\infty$ OLS methodology was extended to the flexible launch vehicle case, resulting in a Simultaneous Attitude Controller/Bending Filter $\mathcal{H}_\infty$ OLS design strategy. This new approach was compared to the traditional separate design method, showing that both yield equivalent controllers, with the simultaneous strategy substantially reducing the design effort. Subsequently, a multi-model integrated controller was developed using the integrated approach and tested under both nominal and dispersed conditions. In the (linear) simulations, the controller satisfies all performance and robustness requirements: drift, drift rate and actuation remain well below their limits, the load performance metric stays within acceptable bounds and sufficient stability margins were attained.

These findings indicate that the integrated $\mathcal{H}_\infty$ OLS methodology not only simplifies the controller design process but also yields robust and effective results. The successful performance of the multi-model controller in the evaluated test cases is a strong indicator of the method's potential. Future work will focus on extending the integrated $\mathcal{H}_\infty$ OLS

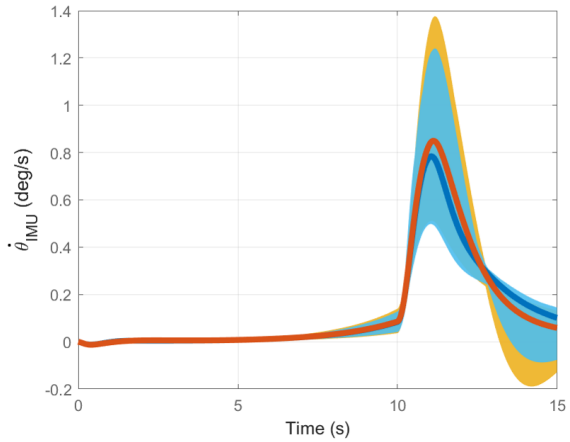

Fig. 22 LFHA Wind - Pitch rate.

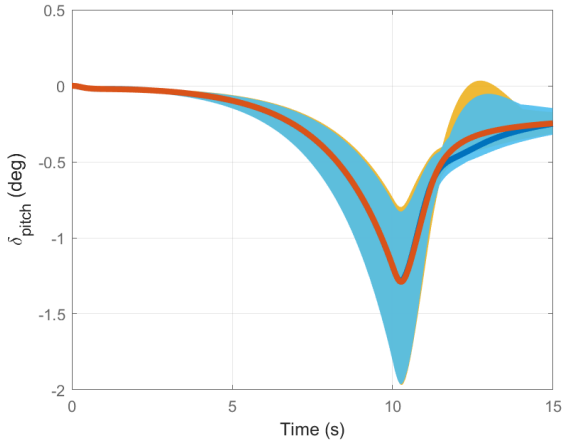

Fig. 23 LFHA Wind - TVC deflection.

methodology to accommodate launch vehicles with sloshing dynamics, and on developing a full-envelope controller to enable nonlinear simulations, aimed at further strengthening the validity of the proposed approach.

References

[1] Tapia, D. N., "Robust and Adaptive TVC Control Design Approaches for the VEGA Launcher," Ph.D. thesis, University of Bristol, 2019.

[2] Simplício, P., Bennani, S., Marcos, A., Roux, C., and Lefort, X., "Structured Singular Value Analysis of the VEGA Launcher in Atmospheric Flight," *Journal of Guidance, Control, and Dynamics*, Vol. vol. 39, No. no. 6, 2016, pp. pp. 1342–1355.

[3] Díaz, E., "Design of a robust controller for the VEGA TVC using the μ synthesis technique," Master's thesis, Universitat Politècnica de Catalunya, 2010.

[4] Klotz, H., "ARIANE 5 DYNAMICS AND CONTROL," *Automatic Control in Aerospace 1992*, IFAC Symposia Series, Pergamon, 1993, pp. pp. 227–233.

[5] Doyle, J. C., "Guaranteed margins for LQG regulators," *IEEE Transactions on Automatic Control*, Vol. vol. AC-23, No. no. 4, 1978, pp. pp. 756–757.

[6] Diz, J. T., Simplício, P., and Theodoulis, S., "$\mathcal{H}_\infty$ Loop Shaping for Robust Attitude Control of Launch Vehicles," *Proceedings of ROCOND 2025*, 2025. Unpublished.

[7] Simplício, P., "Guidance and Control Elements for Improved Access to Space from Planetary Landers to Reusable Launchers," Ph.D. thesis, University of Bristol, 2019.

[8] Bernard, M., "VEGA missionization and post flight analyses," Ph.D. thesis, Sapienza Universita di Roma, Italy, 2009.

[9] Greensite, A. L., "Analysis and Design of Space Vehicle Flight Control Systems. Volume VII - Attitude Control During Launch," NASA Contractor Report CR-826, NASA, 1967.

[10] Vidyasagar, M., and Kimura, H., "Robust controllers for uncertain linear multivariable systems," *Automatica*, Vol. vol. 22, No. no. 1, 1986, pp. pp. 85–94.

[11] McFarlane, D., Glover, K., and Noton, M., "Robust stabilization of a flexible space-platform: An $\mathcal{H}_\infty$ coprime factorization approach," *Proceedings 1988 International Conference on Control*, Oxford, 1988.

[12] McFarlane, D., and Glover, K., "An $\mathcal{H}_\infty$ design procedure using robust stabilization of normalized coprime factors," *Proceedings 1988 Conference on Decision and Control*, 1988.

[13] Glover, K., and McFarlane, D., "Robust stabilization of normalized coprime factor plant descriptions with $\mathcal{H}_\infty$ -bounded uncertainty," *IEEE Transactions on Automatic Control*, Vol. vol. 34, No. no. 8, 1989, pp. pp. 821–830.

[14] McFarlane, D., *Robust controller design using normalized coprime factor plant descriptions*, Lecture Notes in Control and Information Sciences, Springer, New York, 1989.

[15] McFarlane, D., and Glover, K., "A loop-shaping design procedure using $\mathcal{H}_\infty$ synthesis," *IEEE Transactions on Automatic Control*, Vol. vol. 37, No. no. 6, 1992, pp. pp. 759–769.

[16] Papageorgiou, G., "Robust Control System Design: $\mathcal{H}_\infty$ Loop Shaping and Aerospace Applications," Dissertation for the degree of doctor of philosophy, Darwin College, Cambridge, 1998.

[17] Skogestad, S., and Postlethwaite, I., *Multivariable Feedback Control: Analysis and Design*, John Wiley & Sons, 2005.

[18] Marcos, A., Bates, D., and Postlethwaite, I., "Control oriented uncertainty modelling using μ sensitivities and skewed μ analysis tools," *Proceedings of the 44th IEEE Conference on Decision and Control*, 2005, pp. pp. 6436–6441.